Implementation of full *ab initio* band calculation of frequency-dependent third-order nonlinear optical susceptibilities: a sum-over-states calculation

You-Zhao Lan*[1]

Institute of Physical Chemistry, College of Chemistry and Life Sciences, Zhejiang Normal University, Zhejiang, Jinhua 321004, China

Abstract

We implement the full *ab initio* band calculation of the frequency-dependent third-order nonlinear optical susceptibility for the third harmonic generation process in the whole Brillouin zone on the basis of the sum-over-states formulation by Aversa and Sipe [Phys. Rev. B 52, 14636 (1995)]. The implementation was made to satisfy the intrinsic permutation symmetry and applied to calculate the frequency-dependent third harmonic generation of cubic silicon bulk. The accurate all-electron full potential linearized augmented plane wave method was used to calculate the energy band structure and momentum matrix elements. Both real and imaginary parts of susceptibility were directly calculated and checked by the Kramers–Kronig relation. Compared to theoretical results based on the two-band model and semi-empirical band calculations, our present results shows an improvement and agree well with recent theoretical results based on the *ab initio* real-time-based computational approach. The electronic origin of nonlinear optical response contributed from interband and intraband motion was analyzed by tracing the sum-over-states process. The single-particle transition channels with a significant contribution to the nonlinear response coefficients were identified.

[1] Corresponding author: Youzhao Lan; Postal address: Institute of Physical Chemistry, College of Chemistry and Life Sciences, Zhejiang Normal University, Zhejiang, Jinhua 321004, China; Fax: +086 579 82282269; E-mail address: lyzhao@zjnu.cn

1. Introduction

In the last three decades, the perturbation-theory-based sum-over-states (SOS) method [1] has been widely used to calculate the optical polarizability of isolated atoms or molecules [2–4]. Using the SOS method, one can not only carry out the frequency-dependent optical response calculation but also investigate the electronic origin of the optical response. The former produces the theoretical results that more directly compared to experiments, as the nonlinear optical measurements are performed at different optical frequencies. The latter is helpful in identifying which excited states play a significant role in the optical response, then analyzing the charge transition contribution to these selective excited states, and ultimately identifying which functional groups dominate the optical response of the whole molecule. The corresponding findings will guide us to design and synthesize the material with a large nonlinear optical response [2,3].

For condensed semiconductor materials, the SOS method has also been developed to determine their linear and nonlinear optical susceptibilities [5–11]. For the linear optical susceptibility $\chi^{(1)}$, we can easily implement the SOS calculations providing that the band structure and momentum matrix elements are obtained. For the nonlinear optical susceptibilities such as $\chi^{(2)}$ and $\chi^{(3)}$, however, the difficulty increases rapidly owing to the complexity of the equations [6,7,9–15]. For $\chi^{(2)}$, the theoretic technique has been developed to a rather sophisticated level for both static and dynamic cases. At the outset, the static and dynamic calculations were separately developed because merging the static ($\omega \rightarrow 0$) calculation into the dynamic one was hindered by apparently diverging terms in the SOS equations [13,14,16,17] (i.e., factors of ω^{-1} and ω^{-2}). To overcome the difficulty of unphysical divergences, Sipe and Ghahramani (SG) [10] developed the formalism for calculating the nonlinear optical coefficients within the independent-particle

approximation. SG eliminated the unphysical divergences by a carefully separate treatment of interband and intraband motion and provided the detailed expressions for the calculation of second harmonic generation. These detailed expressions have been widely used to calculate the second harmonic generation coefficients of semiconductors [6–9,11,18]. These calculations provide much valuable information to understand the second order nonlinear optical response of semiconductors.

For $\chi^{(3)}$, application of the SOS technique is much less than for $\chi^{(2)}$ because of the complexity of equations. The connection between static and dynamic calculation was also plagued by the apparently diverging term [12,15]. SG has pointed that the divergence-free expressions of $\chi^{(3)}$ can be developed in a similar way to $\chi^{(2)}$ but the derivation will be a formidable task. On the other hand, also within the independent-particle approximation, by applying the perturbation theory to the dynamical equation of the electronic density operator and using a so-called length-gauge formulation, Aversa and Sipe (AS) [5] presented well-behaved, general expressions for $\chi^{(2)}$ and $\chi^{(3)}$ for arbitrary frequency mixings in a simpler way than SG. The expressions for $\chi^{(2)}$ are in well consistent with those shown in SG. Significantly, the derivation of expressions for $\chi^{(3)}$ from AS requires much fewer efforts than from SG. The expressions for $\chi^{(3)}$ were given explicitly in the divergence-free form. Clearly, these expressions are also helpful in understanding the third-order nonlinear optical response of semiconductors. However, to our best knowledge there has been no implementation of $\chi^{(3)}$ based on these expressions so far. Although there are a few reports [12,15] about calculations of $\chi^{(3)}$ based on the SOS method, these works are based on the two-band or empirical and semi-*ab initio* band models. The more accurate band model calculations are required for the calculation of $\chi^{(3)}$ which is highly sensitive to the details of the band structures and wave functions [15].

The purpose of this work is two-fold. One is to fully implement the AS formulism [5] to calculate the $\chi^{(3)}$ and to illustrate its application to bulk silicon. The other is to use the accurate all-electron full potential linearized augmented plane wave (FP-LAPW) method [19–21] within the local density approximation to perform the full *ab initio* band model calculation of $\chi^{(3)}(\omega)$. The calculated results are in agreement with the recent ones [22] based on an *ab initio* real-time-based computational approach combined with the Berry-phase formulation of the dynamical polarization. By tracing the SOS process, we easily extract the transition term with a significant contribution to nonlinear coefficients and identify the ω, 2ω, or 3ω resonant contributions to the peak in the frequency-dependent nonlinear optical spectra.

In Sec. 2, we outline the formalism of AS and point out several critical points of implementation. In Sec. 3, the computational details for an application to silicon bulk are given. In Sec. 4, we discuss the scissor correction, k-point convergence, and Kramers–Kronig relation tests of $\chi^{(3)}(\omega)$, and compare our results with other theoretical ones as well as experiments, and analyze the origin of interband and intraband contributions to $\chi^{(3)}(\omega)$. Finally, we summarize our results in Sec. 5.

2. Formalism and implementation

The equations used to calculate the third-order response function were originally obtained by AS [5] who used the length-gauge formalism based on the position operator **r** (Ref.[23]). For convenience of reading, we inherit the AS's notations. The third-order susceptibility tensor represented by $\chi^{(3)}{}_{dcba}(-\omega_3;\omega_\gamma,\omega_\beta,\omega_\alpha)$, where $\omega_3=\omega_\gamma+\omega_\beta+\omega_\alpha$, is decomposed to $\chi^{(3)}{}_{\chi}$ and $\chi^{(3)}{}_{\sigma}$ based on the decomposition of the physical contributions to the polarization [5], namely, $d\mathbf{P}/dt = d\mathbf{P}_\chi/dt$

+ $\mathbf{J}_\sigma$. The final expressions for $\chi^{(3)}{}_\chi$ and $\chi^{(3)}{}_\sigma$ are as follows:

$$\begin{aligned}\frac{\chi^{(3)}_{\chi,dcba}}{C} = & \sum_{l,m,n,p,k} \frac{r^d_{mn}}{\omega_{nm}-\omega_3}\left[\frac{r^c_{nl}}{\omega_{lm}-\omega_2}\left(\frac{r^b_{lp}r^a_{pm}f_{mp}}{\omega_{pm}-\omega_1}-\frac{r^a_{lp}r^b_{pm}f_{pl}}{\omega_{lp}-\omega_1}\right)-\left(\frac{r^b_{nl}r^a_{lp}f_{pl}}{\omega_{lp}-\omega_1}-\frac{r^a_{nl}r^b_{lp}f_{ln}}{\omega_{nl}-\omega_1}\right)\frac{r^c_{pm}}{\omega_{np}-\omega_2}\right] \\ & + i\sum_{l,m,n,k} \frac{r^d_{mn}}{\omega_{nm}-\omega_3}\left[\frac{1}{\omega_{nm}-\omega_2}\left(\frac{r^b_{nl}r^a_{lm}f_{ml}}{\omega_{lm}-\omega_1}-\frac{r^a_{nl}r^b_{lm}f_{ln}}{\omega_{nl}-\omega_1}\right)\right]_{;k^c} \\ & + i\sum_{l,m,n,k} \frac{r^d_{mn}}{\omega_{nm}-\omega_3}\left[\frac{r^c_{nl}}{\omega_{lm}-\omega_2}\left(\frac{r^a_{lm}f_{ml}}{\omega_{lm}-\omega_1}\right)_{;k^b}-\left(\frac{r^a_{nl}f_{ln}}{\omega_{nl}-\omega_1}\right)_{;k^b}\frac{r^c_{lm}}{\omega_{nl}-\omega_2}\right] \\ & - \sum_{m,n,k} \frac{r^d_{mn}}{\omega_{nm}-\omega_3}\left[\frac{1}{\omega_{nm}-\omega_2}\left(\frac{r^a_{nm}f_{mn}}{\omega_{nm}-\omega_1}\right)_{;k^b}\right]_{;k^c}\end{aligned} \tag{1}$$

and

$$\begin{aligned}\frac{\chi^{(3)}_{\sigma,dcba}}{C} = & \sum_{mnk}\frac{1}{\omega_{mn}-\omega_2}\left(\frac{r^c_{nm}}{\omega_{mn}+\omega_3-\omega_2}\right)_{;k^d}\left(\frac{r^a_{mn}f_{nm}}{\omega_{mn}-\omega_1}\right)_{;k^b} \\ & + i\sum_{lmnk}\frac{r^a_{mn}r^b_{lm}}{\omega_{ln}-\omega_2}\left(\frac{f_n}{\omega_{mn}-\omega_1}+\frac{f_l}{\omega_{lm}-\omega_2+\omega_1}\right)\left(\frac{r^c_{nl}}{\omega_{nl}-\omega_3+\omega_2}\right)_{;k^d}\end{aligned} \tag{2}$$

where $C = e^4K/\hbar^3$ with the K factor depending on the particular combination [1] of ω_γ, ω_β, and ω_α, for example, K is 1/4 for the third harmonic generation (THG) polarizability $\chi^{(3)}{}_{dcba}(-3\omega;\omega,\omega,\omega)$, ω_1 and ω_2 are defined by $\omega_1 = \omega_\alpha$ and $\omega_2 = \omega_\alpha + \omega_\beta$, respectively. $\omega_{mn} = \omega_m - \omega_n$ is the energy difference between the bands m and n, $f_{mn} = f_m - f_n$ is the difference of the Fermi distribution functions, the indices of a, b, and c are Cartesian directions, and all four band indices l, m, n, p are different (one exception is shown below) because r_{mn} [$= p_{mn}/(im\omega_{mn})$] is defined to be zero unless $n \neq m$ (Ref.[5]). So, to calculate the $\chi^{(3)}{}_{dcba}$ by using Eqs.1 and 2, we first have to obtain the band structure of periodic system and the momentum matrix elements.

As mentioned by AS, Eqs.1 and 2 remain to be symmetrized to satisfy the intrinsic permutation symmetry, that is, invariance under the possible permutations of (a, ω_α), (b, ω_β), and (c, ω_γ). Here, we focus on the THG polarizability $\chi^{(3)}{}_{dcba}(-3\omega;\omega,\omega,\omega)$ whose intrinsic permutation symmetry can be readily performed by

$$\chi^{(3)}_{dcba}\left(-3\omega;\omega,\omega,\omega\right)=\frac{1}{6}\left[\begin{array}{l}\chi^{(3)}_{dcba}\left(-3\omega;\omega,\omega,\omega\right)+\chi^{(3)}_{dcab}\left(-3\omega;\omega,\omega,\omega\right)+\chi^{(3)}_{dbca}\left(-3\omega;\omega,\omega,\omega\right)\\+\chi^{(3)}_{dbac}\left(-3\omega;\omega,\omega,\omega\right)+\chi^{(3)}_{dabc}\left(-3\omega;\omega,\omega,\omega\right)+\chi^{(3)}_{dacb}\left(-3\omega;\omega,\omega,\omega\right)\end{array}\right] \quad (3)$$

During the implementation of Eqs.1 and 2, the frequency ω should be understood as $\omega + i\eta$ with a small positive η value (general 0.005 a.u.) and the following expressions were used,

$$\Delta^a_{nm}\equiv\left(\omega_{nm}\right)_{;k^a}=\left(p^a_{nn}-p^a_{mm}\right)/m \quad (4)$$

$$\left(\frac{r^a_{nm}}{\omega_{nm}-\omega_1}\right)_{;k^b}=\frac{r^a_{nm;k^b}}{\omega_{nm}-\omega_1}-\frac{r^a_{nm}\Delta^b_{nm}}{\left(\omega_{nm}-\omega_1\right)^2} \quad (5)$$

$$r^b_{nm;k^a}=\frac{r^a_{nm}\Delta^b_{mn}+r^b_{nm}\Delta^a_{mn}}{\omega_{nm}}+\frac{i}{\omega_{nm}}\sum_{l\neq n,m}\left(\omega_{lm}r^a_{nl}r^b_{lm}-\omega_{nl}r^b_{nl}r^a_{lm}\right) \quad (6)$$

$$\Delta^b_{nm;k^a}=\sum_l\left[\omega_{lm}\left(r^a_{ml}r^b_{lm}+r^b_{ml}r^a_{lm}\right)-\omega_{ln}\left(r^a_{nl}r^b_{ln}+r^b_{nl}r^a_{ln}\right)\right] \quad (7)$$

where the ;**k** operator represents a generalized derivative introduced by AS and **p** is momentum operator.

There is no obvious divergence in Eqs.1 and 2 except that the first summation of Eq.1 shows an apparent divergence arising from both a lack of r_{lm} and r_{np} elements in numerators and a factor of $1/\omega_2$ for $\chi^{(3)}_{dcba}(0;0,0,0)$ when $l = m$ and $n = p$. Introducing intrinsic permutation symmetry and relabeling indices, we reduced these two troublesome terms (TTT) to

$$\chi^{(3),\mathrm{TTT}}_{\chi,dcba}=C\sum_{l,m,n,k}f_{ml}\left[\frac{r^d_{nm}r^c_{mn}}{\left(\omega_{mn}-\omega_3\right)}-\frac{r^c_{nm}r^d_{mn}}{\left(\omega_{nm}-\omega_3\right)}\right]\left[\frac{r^b_{ml}r^a_{lm}}{\left(\omega_{lm}-\omega_1\right)\left(\omega_{lm}+\omega_2-\omega_1\right)}\right] \quad (8)$$

In evaluation of the matrix elements r_{mn} as $p_{mn}/(im\omega_{mn})$, a numerical problem occurs when the bands m and n are nearly degenerate. As mentioned by AS, one can always choose the appropriate wave functions for the bands m and n such that the matrix elements r_{mn} (or p_{mn}) vanishes. Therefore, for nearly degenerate bands m and n decided by a small cutoff value, e.g., $\omega_{mn} \leq 0.001$ a.u., we set r_{mn} to be zero, in consistent with the definition of r_{mn} above. This strategy was smoothly used by Rashkeev *et al.* [7] in their calculations of frequency-dependent

second-order optical response of semiconductors.

3. Computational details

We applied our implementation to the calculation of THG of cubic silicon crystal (Si) with a lattice parameter of 5.43Å. The wave functions and momentum matrix elements were computed with the highly accurate all-electron FP-LAPW method [19–21] within the local density approximation as implemented in the ELK code [24]. Since the LDA calculation underestimates the band gap of Si, we applied the widely used scissor correction [25] in the optical calculation. Both the real and imaginary parts of $\chi^{(3)}$ were directly calculated and checked by the Kramers–Kronig relation (KKR) [26]. The maximum angular momentum used for APW functions is $l_{\max} = 8$. Since the nonlinear optical calculation requires much denser k-point mesh than the linear optical calculation [6,9], we performed the convergence tests of $\chi^{(3)}$ with the 10×10×10, 20×20×20, 30×30×30, and 40×40×40 k-point meshes. In terms of the limit of cubic symmetry, we only calculated two nonzero independent elements of $\chi^{(3)}$, namely, $A \equiv \chi^{(3)}_{1111}$ and $B \equiv 3\chi^{(3)}_{1212}$, and their anisotropy $\sigma \equiv (B - A)/A$ that vanishes for isotropic media.

4. Applications

4.1 Scissor correction

It is well known that the LDA underestimates the band gap in semiconductors. Since the denominators of Eqs.1 and 2 depend on the $1/\omega^4_{nm}$ like factors, the underestimation of the band gaps definitely leads to an error in calculation of $\chi^{(3)}$. It is known that the errors are 10–20% and 30–40% orders in calculations of the linear and second-order nonlinear responses [6,7,25,27],

respectively. The simple and effective way is to introduce a so-called scissor correction, in which the band energies are shifted by a factor of $\Delta\omega$ and the momentum matrix elements are corrected by $p_{mn} = p_{mn}(1+f_{mn}\Delta\omega/\omega_{nm})$ (Ref.[25]). The scissor correction is derived by adding to the LDA Hamiltonian the scissor operator that is an effective self-energy [27,28]. The $f_{mn}\Delta\omega/\omega_{nm}$ is considered as a nonlocal contribution to the matrix element [27,28], in consistent with a point of view of the nonlocal exact density functional [29]. This nonlocal correction may have a significant contribution to the matrix element, as shown by Nastol *et al.* [25]. Their estimation for GaAs had shown that the $\Delta\omega/\omega_{nm}$ value is about 4.4 for a lowest conduction band *n*, and a highest valence band *m* near the Γ point. As shown in calculations of $\chi^{(2)}$ of GaAs and GaP, the magnitude of $\chi^{(2)}$ was dramatically improved by applying the scissor correction [25]. Using the FP-LAPW/LDA method, we obtain for Si an indirect gap of 0.46 eV which is lower by 0.69 eV than the experimental value of 1.15 eV. In the following calculations of $\chi^{(3)}$ we used a scissor correction of 0.69 eV.

4.2 Convergence test

The calculations of $\chi^{(2)}$ [7,9] have shown that a denser k-point mesh is required for nonlinear than linear optical properties in the irreducible Brillouin zone (IBZ). We performed the convergence tests with the 10×10×10, 20×20×20, 30×30×30, and 40×40×40 k-point meshes corresponding to 47, 256, 752, and 1661 k-points in IBZ. Figure 1 shows the LDA absolute values of $\chi^{(3)}_{1111}(\omega)$ for different k-point meshes. For comparison, we also show the $\varepsilon_2(\omega)$ (the real part of dielectric constant) calculated by using the following expression [5,10],

$$\varepsilon_{ba}(\omega) = \delta_{ba} + 4\pi \frac{e^2}{\hbar} \sum_{n,m,k} \frac{r^b_{mn} r^a_{nm} f_{mn}}{\omega_{nm} - \omega} = \varepsilon_1(\omega) + i\varepsilon_2(\omega) \qquad (9)$$

As shown in Fig. 1, the $\varepsilon_2(\omega)$ exhibits a better convergence than the $\chi^{(3)}_{1111}(\omega)$ in a wide energy

region. In the static case, the calculated $\varepsilon_1(0)$ values for four k-points meshes (10×10×10, 20×20×20, 30×30×30, and 40×40×40) are 12.25, 11.91, 11.91, and 11.91, respectively, in good agreement with the experimental value of 12.0, while for $\chi^{(3)}_{1111}(0)$ they are separately 0.23×10^{-10}, 2.41×10^{-10}, 5.22×10^{-10}, and 6.43×10^{-10} esu, which has presented a convergence trend. The $\chi^{(3)}_{1111}(0)$ based on the 10×10×10 k-point mesh seems to be close to the only available experimental value of $\chi^{(3)}_{1111}(0)$ that is $(0.24 \pm 60\%) \times 10^{-10}$ esu estimated by Moss *et al.*[15] from the dynamic experimental measurement [30]. Actually, as will be shown in Subsection 4.4, there is no good agreement between all the theoretical results and experiments. Although a well convergence has not been obtained in the static case, in the dynamic case (ω > 0.5eV), the $\chi^{(3)}_{1111}(\omega)$ values present a good convergence for four k-points meshes and agree with recently calculated results [22] based on an *ab initio* real-time-based computational approach. For $\chi^{(3)}_{1212}(\omega)$, we obtain a similar behavior for convergence test. In the following section, we will use the 30×30×30 results to make further discussions.

4.3 KKR test

The KKR [26,31,32] describes a general connection between the real and imaginary parts of complex optical functions. In previous researches on nonlinear optical calculations [7,15,33], to reduce the computational efforts, one often only calculated the imaginary part of optical function and used the KKR to calculate its real part. As shown in Eqs.1 and 2, the strategy based on the KKR of $\chi^{(3)}(\omega)$ does not simplify the calculation because the full extract of the imaginary parts of $\chi^{(3)}(\omega)$ is also very complicated. So we directly calculated the real and imaginary parts of $\chi^{(3)}(\omega)$ and used the KKR to check the validity of results. For THG, the real and imaginary parts of $\chi^{(3)}(\omega)$ satisfy the following KKR [26],

$$\mathrm{Re}\left\{\chi^{(3)}_{dcba}\left(-3\omega_1;\omega_1,\omega_1,\omega_1\right)\right\}=\frac{2}{\pi}\int_0^{\infty}\frac{\omega_2\,\mathrm{Im}\left\{\chi^{(3)}_{dcba}\left(-3\omega_2;\omega_2,\omega_2,\omega_2\right)\right\}}{\omega_2^2-\omega_1^2}d\omega_2 \qquad (10)$$

As an example, we shows in Fig. 2 the dispersions of the directly calculated real and imaginary parts of $\chi^{(3)}{}_{1111}(\omega)$ and of the real part of $\chi^{(3)}{}_{1111}(\omega)$ based on the KKR calculation. It is clearly shown that the directly calculated results are in well consistent with the KKR ones, which supports our correct implementations of Eqs.1 and 2.

4.4 Comparisons with other theoretical results and experiments

To get a better evaluation for our results, we compare our results with other theoretical reports [15,22,34–36] as well as experiments [30,37]. In Fig. 3, we compare our results based on 30×30×30 k-points with those based on the tight-binding with either semi-*ab-initio* (STB) or empirical parameters (ETB) as well as based on an *ab initio* real-time-based computational approach combined with the Berry-phase (BP) formulation of the dynamical polarization. And for clarity, we list in table 1 the theoretical and experimental values of $\chi^{(3)}{}_{1111}(\omega)$ ($\times 10^{-10}$ esu) at ω = 0.0 and 1.16 eV. Overall, there are apparent differences between different theoretical values and between theoretical and experimental values. In the static case, Jha and Blqembergen [35] obtained a negative $\chi^{(3)}{}_{1111}(0)$ value of -0.25×10^{-10} esu within the completely-localized-bond approximation on the basis of simple tetrahedral bonding orbitals. They obtained a negative $\chi^{(3)}{}_{1111}(0)$ value owing to the vanishment of the term including matrix elements between bonding-bonding or anti-bonding-anti-bonding states in the limitation of the center-of-inversion symmetry of Si. Since this negative theoretical value dramatically differs from available experimental values [30,37], using a tight-binding model with retaining more interactions between bonds, Arya and Jha [34] appeared to obtain largely improved results for $\chi^{(3)}{}_{1111}(0)$, however, these results are not so good as concluded by Arya and Jha because they used a different definition as

pointed by Moss *et al.*(See. ref.24 of [15]). Significantly, by considering the intraband Franz-Keldysh effect to calculate $\chi^{(3)}(\omega)$, Vechten and Aspnes [36] obtained a largely improved value of 0.20×10^{-10} esu in good agreement with the experimental value as shown in table 1, even though they included only two bands ($\Gamma_{25'}$ and Γ_{15} of Si). Their work also implies an importance of intraband contributions especially for crystals with small energy gaps. As a further improvement, Moss *et al.* [15] used both an empirical tight-binding (ETB) and a semi-*ab-initio* band structure technique with standard perturbation theory to calculate the $\chi^{(3)}(\omega)$ and obtained the results with a better agreement with the static experimental value. Note that there is a large uncertainty (±60%) in the static experimental value (table 1), which leads to the results ranging from 0.096×10^{-10} to 0.384×10^{-10} esu. For the dynamic case, as shown in table 1, all the theoretical values at ω = 1.16 eV dramatically deviate from the experimental value. However, from Fig. 3, we observe that all the theoretical methods yield a similar dispersion with $\omega > 0.5$ eV and the dispersion presents a peak due to a possible 2ω or 3ω resonance near 1.3 eV. It should be noted that there is also a large uncertainty (±50%) in this experimental value and the measurement is often performed relative to a reference sample. So a direct comparison between theoretical and experiment values is often difficult [2].

For cubic Si with diamond structure, the anisotropy (σ defined above) of $\chi^{(3)}(\omega)$ is another parameter of interest [15,30,37,38]. Figure 4 shows the dispersion of $|\sigma(\omega)|$ based on experiments and different theoretical calculations. In the static case, both ETB and ours are in agreement with experiments, while in the dynamic case, all the theoretical calculations only partly agree with experiments. For example, at ω = 0.8 – 1.4 eV, the BP results and ours present a better agreement with experiments than other theoretical ones, and so do the BP and ETB results at ω = 0.5 – 0.8 eV,

Additionally, at ω = 1.1 and 1.4 eV, two peaks present in experimental data are also shown in the ETB results with ω = 1.1 and 1.5 eV. A possible reason for such different theoretical results is the strong dependence of σ on the electronic band structure [15].

4.5 Interband and Intraband contributions

It has been found that the intraband contribution is important in nonlinear optical responses [15,36]. Figure 5 shows the dispersions of interband and intraband contributions of $\chi^{(3)}(\omega)$. In terms of the decomposition of position operator ($r = r_i + r_e$, r_i and r_e are intraband and interband parts of r) [5], Eq.1 related to the interband part r_e is referred to as the interband contribution while Eq.2 related to the intraband part r_i is the intraband contribution (Jintra in Fig.5). Note that the later three summations of Eq.1 also contain diagonal momentum matrix elements (p_{nn} of Eq.4). So the later three summations of Eq.1 is considered as a mixture of intraband and interband contributions (Pmix in Fig.5) while the first summation of Eq.1 is the pure interband contribution (Pinter in Fig.5) that does not contains diagonal momentum matrix elements.

As shown in Fig.5, Pinter is smaller by an order of magnitude than both Pmix and Jintra, and at low frequencies Jintra has a larger contribution than both Pinter and Pmix, in consistent with the fact of important intraband contributions in nonlinear optical responses [15,36]. The $\mathrm{Re}[\chi^{(3),\mathrm{Pinter}}{}_{1111}(\omega)]$ presents two peaks at ω = 1.55 and 2.16 eV. To understand the origin of these two peaks, we traced the SOS calculations in terms of Eq.1 for these two applied frequencies. Figure 6 shows the trace of summation over all 27000 (30×30×30) k-points for $\mathrm{Re}[\chi^{(3),\mathrm{Pinter}}{}_{1111}(\omega)]$ with ω = 1.55 and 2.16 eV. We observed that a great number of k-points almost have no contribution to $\mathrm{Re}[\chi^{(3)}{}_{1111}(\omega)]$. In detail, we show the distribution of contribution for each k-point in summation as insets of Fig. 6, where only absolute contributions larger than 1.0 a.u. are given

for clarity. From insets, we can see that a few k-points (labeled by a, b, c1, c2, d1, d2, e1, e2, f1, and f2) have a relative large contribution to Re[$\chi^{(3),\mathrm{Pinter}}{}_{1111}(\omega)$]. To check whether these relative large contributions are attributed to the possible ω, 2ω, or 3ω resonance in Pinter of Eq.1, we separately traced the SOS calculations for these k-points. Table 2 lists the single-particle channels with significant contributions to each k-point. Eq.11 shows the calculating expression for Pinter obtained by rearranging the dummy indices.

$$\begin{aligned}\frac{\chi_{\chi}^{(3)\mathrm{Pinter}}}{C} &= \sum_{l,m,n,p,k} \frac{r_{mn}^{d}}{\omega_{nm}-\omega_3}\left[\frac{r_{nl}^{c}}{\omega_{lm}-\omega_2}\left(\frac{r_{lp}^{b}r_{pm}^{a}f_{mp}}{\omega_{pm}-\omega_1}-\frac{r_{lp}^{a}r_{pm}^{b}f_{pl}}{\omega_{lp}-\omega_1}\right)-\left(\frac{r_{nl}^{b}r_{lp}^{a}f_{pl}}{\omega_{lp}-\omega_1}-\frac{r_{nl}^{a}r_{lp}^{b}f_{\ln}}{\omega_{nl}-\omega_1}\right)\frac{r_{pm}^{c}}{\omega_{np}-\omega_2}\right] \\ &= f_{mn}\sum_{l,m,n,p,k}\left[\frac{r_{mp}^{d}}{\omega_{pm}-\omega_3}\frac{r_{pl}^{c}}{\omega_{lm}-\omega_2}\frac{r_{\ln}^{b}r_{nm}^{a}}{\omega_{nm}-\omega_1}-\frac{r_{pl}^{d}}{\omega_{lp}-\omega_3}\frac{r_{\ln}^{c}}{\omega_{np}-\omega_2}\frac{r_{nm}^{a}r_{mp}^{b}}{\omega_{nm}-\omega_1}\right. \\ &\quad \left.-\frac{r_{pl}^{d}}{\omega_{lp}-\omega_3}\frac{r_{mp}^{c}}{\omega_{lm}-\omega_2}\frac{r_{\ln}^{b}r_{nm}^{a}}{\omega_{nm}-\omega_1}+\frac{r_{ln}^{d}}{\omega_{nl}-\omega_3}\frac{r_{pl}^{c}}{\omega_{np}-\omega_2}\frac{r_{nm}^{a}r_{mp}^{b}}{\omega_{nm}-\omega_1}\right]\end{aligned} \tag{11}$$

Combining Eq.11 and these single-particle channels, we may identify which resonance leads to a significant contribution. For instance, for ω = 1.55 eV (0.056 a.u.), the channel of 2(0.1920)→7(0.2946)→8(0.3187)→4(0.1940) with 70% contribution to the final result corresponds to a term of (m = 2)→(n = 7)→(l = 8)→(p = 4) in summation. Inspecting the denominators of Eq.11, we can see that the 2ω resonance leads to a significant contribution because both ω_{lm} (= 0.1267 a.u.) and ω_{np} (= 0.1006 a.u.) are close to ω_2 (= 2ω = 2 × 0.056 = 0.112 a.u.). A similar analysis for ω = 2.16 eV (0.079 a.u.) shows that the 2ω resonance leads to a significant contribution because both ω_{lm} (= 0.1483 a.u.) and ω_{np} (= 0.1561 a.u.) are close to ω_2 (= 2ω = 2 × 0.079 = 0.158 a.u.). For other peaks shown in Fig.5, we can perform similar analyses to check the origin of nonlinear optical response.

In the low applied frequency region, a large $\chi^{(3)}$ value is due to a small energy difference (e.g. ω_{mn}). As shown in Fig.5, Jintra has a large contribution to $\chi^{(3)}(\omega)$ in the low applied frequency region. We traced the SOS calculation in a similar way for the static case. The corresponding

results are shown in Fig.7. Similarly, only parts of 27000 k-points contribute to the Re[$\chi^{(3),Jintra}_{1111}(0)$]. As shown in the inset of Fig.7, several k-points have a large contribution in summation. As examples, we traced the SOS process of two largest values (labeled by *a* and *b* in inset). These two largest values are dominated by the single-particle channels formed by bands 2(0.1796 a.u.), 3(0.1905 a.u.), and 4(0.1933 a.u.). We can see that a small energy difference between bands 3 and 4 (i.e., ω_{34} = –0.0028 a.u.) leads to a large contribution, then to a large Re[$\chi^{(3),Jintra}_{1111}(0)$]. Note that a small energy difference has not led to similar peaks for Pinter and Pmix in the low applied frequency region, as shown in Fig.5. A possible reason is that the Eq.2 for Jintra has (f_{mn}/ω_{mn}) and (f_n/ω_{mn})-like terms while the Eq.1 for Pinter and Pmix only have (f_{mn}/ω_{mn})-like term. As shown in table 2, all the bands of *m* and *n* with a small energy difference ω_{mn} belong to the same band region (valance or conduction band), which leads to a zero value of f_{mn}, then to a zero contribution of f_{mn}/ω_{mn}. However, in the valance band, the (f_n/ω_{mn})-like term still alive because of f_n = 1, which leads to a large f_n/ω_{mn} value. So, the single-particle channels formed by bands 2(0.1796 a.u.), 3(0.1905 a.u.), and 4(0.1933 a.u.) will have a large contribution to Re[$\chi^{(3),Jintra}_{1111}(0)$] owing to the ($f_3/\omega_{34}$) or ($f_4/\omega_{34}$) terms.

5. Conclusions

We have implemented the full *ab initio* band calculation of the frequency-dependent third-order nonlinear optical susceptibility for the third harmonic generation process in the whole Brillouin zone on the basis of the sum-over-states formulation. By using the accurate all-electron FP-LAPW method, theoretical results are improved when compared to the two-band model and semi-empirical band calculations and agree well with recent results based on the *ab initio*

real-time-based computational approach. We applied our implementation to cubic silicon bulk and clearly recognized the origin of peaks in both interband and intraband contributions to nonlinear response coefficients. Our implementation based on the SOS method will be very useful to investigate the mechanism of nonlinear optical response of materials such as two dimensional materials which attract much attention recently [39–45]. For example, for the modified two-dimensional materials such as doped graphenes, we can first identify the bands composing the single-particle channel with a significant contribution to nonlinear response coefficients by tracing the SOS process. Then, we can extract the electronic origin of these bands to check the ability of the modifiers to control the nonlinear optical response. Finally, we can evaluate the effect of modification on the nonlinear response coefficients of materials.

Acknowledgements

We appreciate the financial supports from Natural Science Foundation of China Project 21303164 and the computational supports from Zhejiang Key Laboratory for Reactive Chemistry on Solid Surfaces.

References:

[1] B. J. Orr and J. F. Ward, Mol.Phys. **20**, 513 (1971).

[2] J. L. Brédas, C. Adant, P. Tackx, A. Persoons, and B. M. Pierce, Chem.Rev. **94**, 243 (1994).

[3] D. R. Kanis, M. A. Ratner, and T. J. Marks, Chem.Rev. **94**, 195 (1994).

[4] D. P. Shelton and J. E. Rice, Chem.Rev. **94**, 3 (1994).

[5] C. Aversa and J. E. Sipe, Phys.Rev.B **52**, 14636 (1995).

[6] J. L. P. Hughes and J. E. Sipe, Phys.Rev.B **53**, 10751 (1996).

[7] S. N. Rashkeev, W. R. L. Lambrecht, and B. Segall, Phys.Rev.B **57**, 3905 (1998).

[8] S. Sharma and C. Ambrosch-Draxl, Phys.Scr. **2004**, 128 (2004).

[9] S. Sharma, J. K. Dewhurst, and C. Ambrosch-Draxl, Phys.Rev.B **67**, 165332 (2003).

[10] J. E. Sipe and E. Ghahramani, Phys.Rev.B **48**, 11705 (1993).

[11] J. E. Sipe and A. I. Shkrebtii, Phys.Rev.B **61**, 5337 (2000).

[12] C. Aversa, J. E. Sipe, M. Sheik-Bahae, and E. W. Van Stryland, Phys.Rev.B **50**, 18073 (1994).

[13] Z. H. Levine, Phys.Rev.B **49**, 4532 (1994).

[14] Z. H. Levine, Phys.Rev.B **42**, 3567 (1990).

[15] D. J. Moss, E. Ghahramani, J. E. Sipe, and H. M. van Driel, Phys.Rev.B **41**, 1542 (1990).

[16] Z. H. Levine and D. C. Allan, Phys.Rev.B **44**, 12781 (1991).

[17] Z. H. Levine and D. C. Allan, Phys.Rev.Lett. **66**, 41 (1991).

[18] V. I. Gavrilenko and R. Q. Wu, Phys.Rev.B **65**, 035405 (2001).

[19] Y. Mokrousov, G. Bihlmayer, and S. Blügel, Phys.Rev.B **72**, 045402 (2005).

[20] E. Wimmer, H. Krakauer, and A. J. Freeman, in edited by P. W. Hawkes (Academic Press,

1985), pp. 357–434.

[21] E. Wimmer, H. Krakauer, M. Weinert, and A. J. Freeman, Phys.Rev.B **24**, 864 (1981).

[22] C. Attaccalite and M. Grüning, Phys.Rev.B **88**, 235113 (2013).

[23] E. I. Blount, *Solid State Physics Advances Research Applications* (AcadeAcademic ,New York, 1962).

[24] K. Dewhurst, S. Sharma, L. Nordström, F. Cricchio, F. Bultmark, O. Gräs, and H. Gross, (see http://elk.sourceforge.net/).

[25] F. Nastos, B. Olejnik, K. Schwarz, and J. E. Sipe, Phys.Rev.B **72**, 045223 (2005).

[26] V. Lucarini, J. J. Saarinen, K.-E. Peiponen, and E. M. Vartiainen, *Kramers Kronig Relations Optical Materials Research* (Springer-Verlag Berlin Heidelberg, 2005).

[27] Z. H. Levine and D. C. Allan, Phys.Rev.B **43**, 4187 (1991).

[28] Z. H. Levine and D. C. Allan, Phys.Rev.Lett. **63**, 1719 (1989).

[29] O. Gunnarsson and K. Schönhammer, Phys.Rev.Lett. **56**, 1968 (1986).

[30] J. J. Wynne and G. D. Boyd, Appl.Phys.Lett. **12**, 191 (1968).

[31] H. A. Kramers, in *Attidel Congresso Internazionale DeiFisici* (Zanichelli,Bologna, 1927), pp. 545–557.

[32] R. de L. Kronig, J.Opt.Soc.Am. **12**, 547 (1926).

[33] D. J. Moss, J. E. Sipe, and H. M. van Driel, Phys.Rev.B **36**, 9708 (1987).

[34] K. Arya and S. S. Jha, Phys.Rev.B **20**, 1611 (1979).

[35] S. S. Jha and N. Bloembergen, Phys.Rev. **171**, 891 (1968).

[36] J. A. V. Vechten and D. E. Aspnes, Phys.Lett.A **30**, 346 (1969).

[37] J. J. Wynne, Phys.Rev. **178**, 1295 (1969).

[38] D. J. Moss, H. M. van Driel, and J. E. Sipe, Opt.Lett. **14**, 57 (1989).

[39] I. Al-Naib, M. Poschmann, and M. M. Dignam, Phys.Rev.B **91**, 205407 (2015).

[40] I. Al-Naib, J. E. Sipe, and M. M. Dignam, Phys.Rev.B **90**, 245423 (2014).

[41] J. L. Cheng, N. Vermeulen, and J. E. Sipe, Phys.Rev.B **91**, 235320 (2015).

[42] J. L. Cheng, N. Vermeulen, and J. E. Sipe, NewJ.Phys. **16**, 053014 (2014).

[43] V. A. Margulis, E. E. Muryumin, and E. A. Gaiduk, Phys. Lett. A **380**, 304 (2016).

[44] C.-Y. Wang and G.-Y. Guo, J.Phys.Chem.C **119**, 13268 (2015).

[45] X. Zhou, J. Cheng, Y. Zhou, T. Cao, H. Hong, Z. Liao, S. Wu, H. Peng, K. Liu, and D. Yu, J.Am.Chem.Soc. **137**, 7994 (2015).

List of figure captions:

Figure 1. Convergence tests on $\varepsilon_2(\omega)$ and $\chi^{(3)}(\omega)$ with the 10×10×10, 20×20×20, 30×30×30, and 40×40×40 k-point meshes.

Figure 2. KKR test from imaginary (Im) to real (Re) part of $\chi^{(3)}(\omega)$. The dot and solid lines indicate the directly calculated results while the hollow square indicates the results based on the KKR calculation.

Figure 3. Dispersion of the two independent components of $\chi^{(3)}(\omega)$ based on our strategy, the tight-binding calculations with either semi-*ab initio* (STB) or empirical parameters (ETB), and *ab-initio* approach by means of the dynamical Berry phase (BP).

Figure 4. Dispersion in the magnitude of the anisotropy [$\sigma(\omega) = (3\chi^{(3)}_{1212} - \chi^{(3)}_{1111})/ \chi^{(3)}_{1111}$].

Figure 5. Dispersions of the pure interband (Pinter), a mixture of interband and intraband (Pmix), and intraband (Jinter) contributions of $\chi^{(3)}(\omega)$. P and J indicate $\mathbf{P}_\chi$ and $\mathbf{J}_\sigma$ components, respectively. For clarity, the pure interband contribution is increased by an order of magnitude (*i.e.*, ×10).

Figure 6. Traces of summation over all 27000 (30×30×30) k-points for the real part of $\chi^{(3),\mathrm{Pinter}}_{1111}(\omega)$ with ω = 1.55 and 2.16 eV. Insets are the distribution of contribution (a.u.) per k-point in summation and for clarity only absolute contributions larger than 1.0 a.u. are shown.

Figure 7. Traces of summation over all 27000 (30×30×30) k-points for the real part of $\chi^{(3),\mathrm{Jintra}}_{1111}(0)$. The inset is the distribution of contribution (a.u.) per k-point in summation and for clarity only absolute contributions larger than 500 a.u. are shown.

Table 1. Theoretical and experimental values of $\chi^{(3)}_{1111}(\omega)$ ($\times 10^{-10}$ esu) at ω = 0.0 and 1.16 eV.

	Methods				
	This work	STB	ETB	Other theoretic results	Expt.
ω = 0.0 eV	5.22	0.08	0.48	–0.25 [a], 0.026 [b], 0.20 [c]	0.24 ± 60% [e]
ω = 1.16 eV	0.83	1.3	2.2	0.84 [d]	16.8 ± 50% [f]

[a] Reference [35]

[b] Reference [34]

[c] Reference [36]

[d] BP [22]

[e] Reference [30,37]

[f] This is a relative value measured relative to LiF at the same applied field (ω = 1.16 eV).

Table 2. Selected contributions labeled in insets of Fig. 6 to Re[$\chi^{(3),\mathrm{Pinter}}_{1111}(\omega)$] (a.u.). The single-particle channels with significant contributions to each k-point are given. 2(0.1920) indicates the band 2 with an eigenvalue of 0.1920 a.u. Note that for Si, since the primitive cell includes two silicon atoms and eight valence electrons were considered in calculations, bands 1, 2, 3, and 4 are the valance bands and the rest are conduction bands.

Labels	Contributions [Percentages, Channels (Eigenvalues)]	Final results
ω = 1.55 eV (0.056 a.u.)		
a	–22.52 [70%, 2(0.1920)→7(0.2946)→8(0.3187)→4(0.1940)]	–32.11
	–9.21 [29%, 4(0.1940)→8(0.3187)→7(0.2946)→2(0.1920)]	
b	–23.02 [70%, 2(0.1922)→7(0.2945)→8(0.3185)→4(0.1941)]	–32.75
	–9.35 [29%, 4(0.1941)→8(0.3185)→7(0.2945)→2(0.1922)]	
ω = 2.16 eV (0.079 a.u.)		
c1 and c2	17.31 [42%, 3(0.0839)→6(0.2400)→5(0.2322)→4(0.0859)]	41.36
	23.80 [57%, 4(0.0859)→5(0.2322)→6(0.2400)→3(0.0839)]	
d1 and d2	17.82 [42%, 3(0.0840)→6(0.2398)→5(0.2321)→4(0.0859)]	42.51
	24.42 [57%, 4(0.0859)→5(0.2321)→6(0.2398)→3(0.0840)]	
e1 and e2	17.58 [42%, 3(0.0841)→6(0.2398)→5(0.2319)→4(0.0860)]	42.01
	24.17 [57%, 4(0.0860)→5(0.2319)→6(0.2398)→3(0.0841)]	
f1 and f2	17.08 [42%, 3(0.0840)→6(0.2400)→5(0.2321)→4(0.0860)]	40.88
	23.56 [57%, 4(0.0860)→5(0.2321)→6(0.2400)→3(0.0840)]	

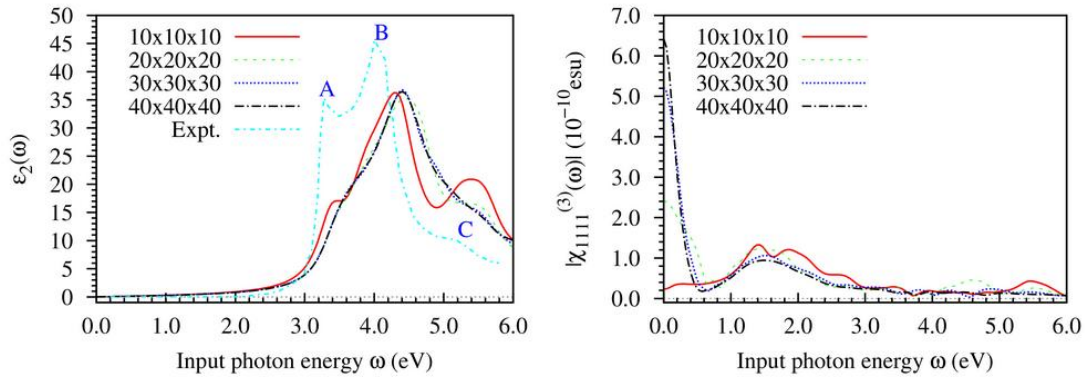

Figure 1. Convergence tests on $\varepsilon_2(\omega)$ and $\chi^{(3)}(\omega)$ with the 10×10×10, 20×20×20, 30×30×30, and 40×40×40 k-point meshes.

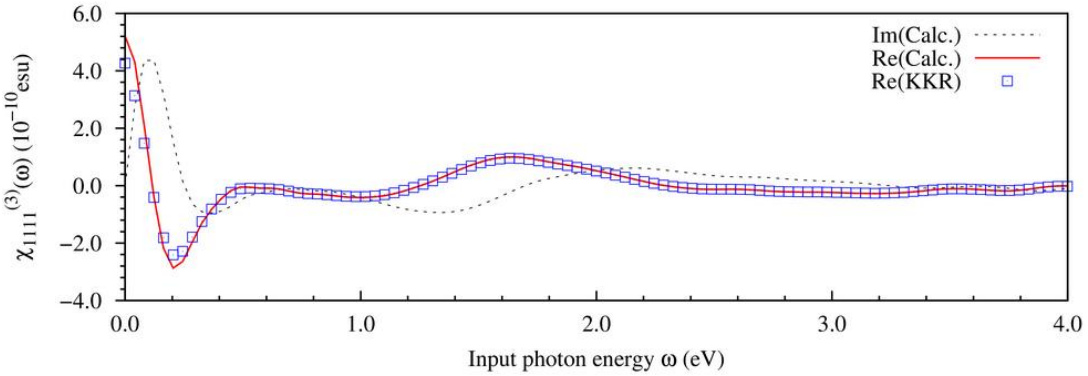

Figure 2. KKR test from imaginary (Im) to real (Re) part of $\chi^{(3)}(\omega)$. The dot and solid lines indicate the directly calculated results while the hollow square indicates the results based on the KKR calculation.

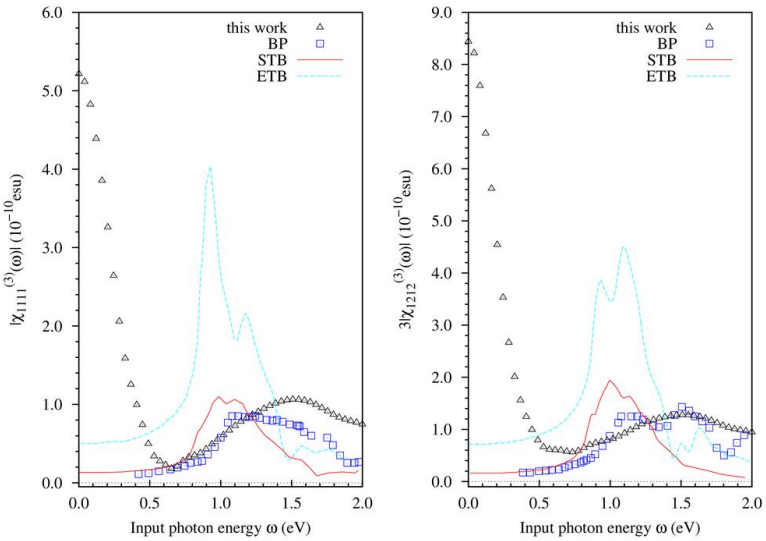

Figure 3. Dispersion of the two independent components of $\chi^{(3)}(\omega)$ based on our strategy, the tight-binding calculations with either semi-*ab initio* (STB) or empirical parameters (ETB), and *ab-initio* approach by means of the dynamical Berry phase (BP).

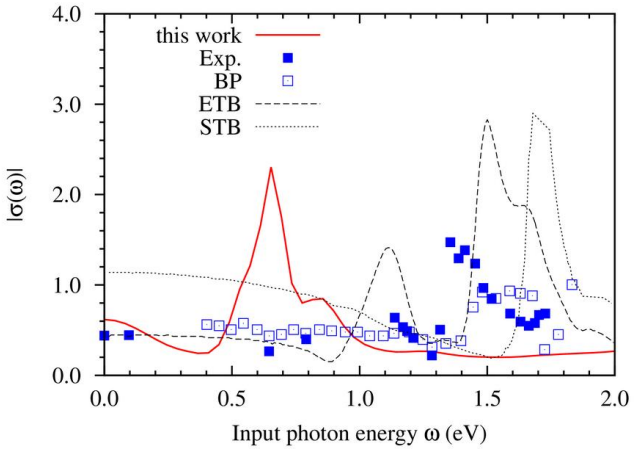

Figure 4. Dispersion in the magnitude of the anisotropy [$\sigma(\omega) = (3\chi^{(3)}_{1212} - \chi^{(3)}_{1111})/ \chi^{(3)}_{1111}$].

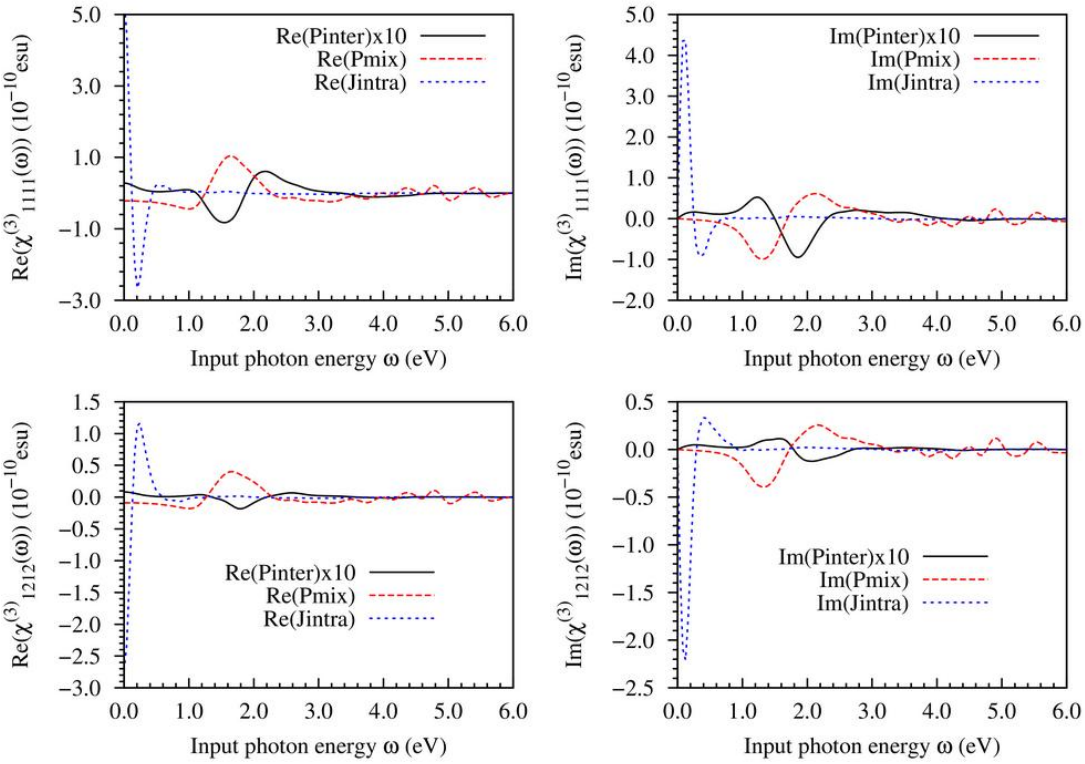

Figure 5. Dispersions of the pure interband (Pinter), a mixture of interband and intraband (Pmix), and intraband (Jinter) contributions of $\chi^{(3)}(\omega)$. P and J indicate $\mathbf{P}_\chi$ and $\mathbf{J}_\sigma$ components, respectively. For clarity, the pure interband contribution is increased by an order of magnitude (*i.e.*, ×10).

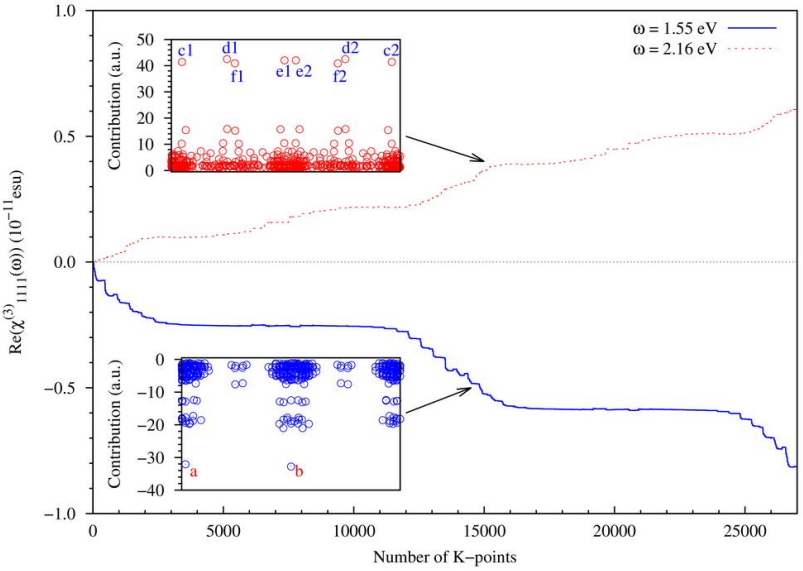

Figure 6. Traces of summation over all 27000 (30×30×30) k-points for the real part of $\chi^{(3),Pinter}_{1111}(\omega)$ with ω = 1.55 and 2.16 eV. Insets are the distribution of contribution (a.u.) per k-point in summation and for clarity only absolute contributions larger than 1.0 a.u. are shown.

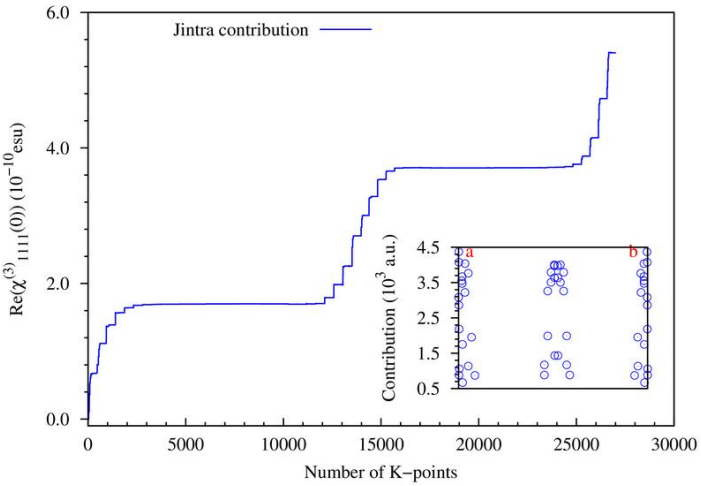

Figure 7. Traces of summation over all 27000 (30×30×30) k-points for the real part of $\chi^{(3),Jintra}_{1111}(0)$. The inset is the distribution of contribution (a.u.) per k-point in summation and for clarity only absolute contributions larger than 500 a.u. are shown.